American Mineralogist, Volume 89, pages 547–553, 2004

A new nondestructive X-ray method for the determination of the 3D mineralogy at the micrometer scale

LAURENCE LEMELLE,[1,*] ALEXANDRE SIMIONOVICI,[1,2] ROBERT TRUCHE,[3] CHRISTOPHE RAU,[2] MARINA CHUKALINA,[2,4] AND PHILIPPE GILLET[1]

[1]Laboratoire de Sciences de la Terre, ENS Lyon, CNRS, UMR5570, 46 allée d'Italie, 69007, Lyon, France
[2]ID22 group, European Synchrotron Radiation Facility (ESRF), 6 rue J. Horowitz, BP 220, F-38043 Grenoble Cedex, France
[3]CEA-DRT-LETI, CEA-Grenoble, 17 rue des Martyrs 38054 Grenoble Cedex 9, France
[4]Institute of Microelectronics Technology RAS, 142432 Chernogolovka, Russia

ABSTRACT

The combination of synchrotron-based X-ray absorption and fluorescence computed tomographies (CT) is a new method allowing a noninvasive and nondestructive determination of the three-dimensional (3D) mineralogy with micrometer resolution of sub-millimeter silicate grains, possibly stored in a silica holder. These CT were performed with beams of a few tens of keV from a third-generation synchrotron source on one olivine grain of the NWA817 Martian meteorite presenting a reddish alteration phase. The reconstructed sections show a network of fractures and a few micrometer-thick layers formed on one grain. The 3D facet orientation and the X-ray attenuation coefficient indicate that this grain is an $Fo_{44\pm9}$ olivine crystal. The fluorescence section reveals rims enriched in Fe (a major element) or depleted in Ca (a minor element). This CT combination shows that the micrometer-thick layer is preferentially formed on the (010) olivine face and has a lower density (3.5 ± 0.4 g/cm^3) than the olivine, even though it is enriched in Fe. Its complex nano-petrography and the distributions of nanometer-sized voids and fractures in such a micrometer thick layer, first observed by scanning electron microscopy on focused ion-beam cuts, is not shown by CT. The precision presently achieved, although moderate, is sufficient to obtain a 3D semi-quantitative view of the mineralogy consistent with the one previously established by electron probe microanalyses (Sautter et al. 2002).

INTRODUCTION

The aim of this paper is to introduce a new method which allows a noninvasive determination of the three-dimensional (3D) mineralogy of a silicate grain with micrometer resolution. This X-ray method is the nondestructive alternative, particularly for sub-millimeter unique grains, to the strategy of extracting small fractions and using them for accurate mineralogical analyses. Because the experiments are carried out in a silica holder, the method is also important to the possibilities for the determination of the mineralogy of grains sampled and sealed in their natural fluid environment. In the near future, extraterrestrial samples possibly collected in and with their atmosphere (i.e., lunar, Martian, or cometary samples) are straightforward examples (Flynn et al. 2000).

With this objective in mind, sub-millimeter silicate grains were analyzed by X-ray absorption and fluorescence tomography using a synchrotron source and by scanning electron microscopy (SEM) coupled with focused ion beam (FIB) techniques. All these cross-sectional imaging techniques were applied to obtain micrometer resolutions, some even beyond their currently established limits, as briefly summarized below. X-ray absorption computed tomography (CT) maps the internal density variations in the target material; its present industrial highest resolution is about 10 µm using an X-ray tube potential of 100 kV on centimeter-sized samples (Ketcham and Carlson 2001). With the advent of third-generation synchrotron sources, the application of fluorescence tomography became possible (Boisseau and Grodzins 1987) and both tomographic techniques approach micrometer-scale resolution (Schroer et al. 2001; Raven et al. 1997). X-ray fluorescence (XRF) computed tomography using a photon beam of a few tens of keV provides information on the 2D/3D elemental distributions. However, XRF is affected by non-negligible attenuation, which has restricted until now the geological applications of XRF CT to the 3D analysis of heavy trace elements in micrometer samples (Sutton et al. 2000). In this work, an XRF correction procedure that takes into account the specific and complex geometry of the sample (Chukalina et al. 2002) was tested on a sub-millimeter mineral grain. The FIB milling put to use in this study to cut a grain requires a protocol slightly different from the one recently employed for extracting TEM specimens (Heaney et al. 2001). As the resolution is determined by both the experimental set-up and the reconstruction algorithms, the comparison at the micrometer-scale of the tomographic reconstructions with the 3D data independently collected using electron beam devices appears the more reliable and pragmatic way to validate the information contained in the generated images and to probe the potential of the proposed imaging method.

Such a comparison was carried out for the cross-sectional images collected from sub-millimeter olivine grains of the NWA817 meteorite, which contains secondary mineralization due to alteration. These grains were chosen because their mineralogy

* E-mail: llemelle@ens-lyon.fr

and petrology are well documented (Sautter et al. 2002; Gillet et al. 2002) for other scientific purposes [NWA817 is a Martian meteorite (McSween 1994)]. The grains are thus advantageous samples for comprehensive 3D imaging exercise. In the first part of this paper, tomographic analyses on a grain stored in a capillary are presented. Then, we present 3D mineralogy and petrology, established up to the nanometer-scale on FIB cuts performed across the alteration phase. They will be discussed only briefly, in view of the very few previously reported observations of the alteration phase at the nanometer scale. The consistency of the tomographic results and the mineralogical potential of the applied combination of tomographic techniques will be specified regarding the electron microprobe results.

EXPERIMENTAL METHOD

Sample

Sub-millimeter-sized olivine grains were extracted from the "North West Africa" (NWA817) meteorite. They were selected visually based on their characteristic shape: subhedral grains elongated along a single axis, having conchoidal fractures and a shape indicating an orthorhombic symmetry. Only the grains presenting reddish alteration phases and colored half red and half green were selected. One of these grains, used in tomographic studies, was stored in a silica capillary and supported by a gold wire placed in the container. The capillary was mounted on a goniometer head. Another grain was dedicated to the FIB preparation.

Although the modal fraction of the olivine is relatively minor in the NWA817 meteorite (about 15%), it has been extensively studied. The main mineralogic and petrographic characteristics have been described by Sautter et al. (2002). The cumulus olivine crystals are anhedral to subhedral with well-developed zoning characterized by an exceptional Fe enrichment and Ca depletion of the marginal overgrowth of the crystals. An average olivine composition of Fo_{40} (Fo_{44} if minor elements are taken into account) was obtained in the core, and Fo_{20} at the surface (see Table 2 in Sautter et al. 2002). The olivines are altered along fractures and grain boundaries, where a reddish Fe-rich silicate phase is formed. All of these results were obtained by optical microscopy, scanning electron microscopy, and electron microprobe studies on thin and polished sections. The presence of phyllosilicates of the smectite family was proposed to explain the X-ray diffraction patterns recorded on the grain sealed in a silica capillary and reported in Gillet et al. (2002).

Scanning electron microscopy on FIB-cuts

Sample cuts were carried out on selected micrometer-sized zones of one grain of the meteorite with a 30 keV Ga FB-2000A Hitachi focused ion beam at the Laboratoire d'Electronique et de Technologie de l'Information of Grenoble (LETI). The samples, coated with amorphous carbon, were scanned with beams of 13 nA in a few 500 μm^2 spots for 10 min, followed by 0.5 nA in a 100 μm^2 spot for 40 min, 130 pA in a 2 μm^2 spot for 10 min, and 17 pA in a 1 μm^2 spot for 5 min. The grains were then carbon-coated, imaged with secondary (4.5 nm resolution) and backscattered electrons (SE and BSE), and analyzed (10 nm probe size) by 20 keV electrons in a Stereoscan 440 (Leo) SEM equipped with an energy dispersive spectrometer. In contrast to the FIB cuts pioneered by Vicenzi and Heaney (1999) on nakhlites, cuts were not performed to take a thin slice for transmission electron microscopy, but to prepare a transverse cut on the bulk grain that could reveal its texture. Using a polished (010) surface of a millimeter-size parallelepiped prepared from a natural San Carlos crystal of olivine (Lemelle et al. 2002), we verified that this technique does not introduce structural artifacts observable by SEM, such as voids or fractures in the first 3.5 μm below the surface.

X-ray computed tomographies

A grain, sealed within a pure silica, air-filled capillary, was studied by high-resolution X-ray absorption and X-ray fluorescence microtomographies on the ID22 beamline of the European Synchrotron Radiation Facility (Simionovici et al. 2000, 2001).

Absorption tomography. For the X-ray absorption tomography (Rau et al. 2001), a monochromatic beam of 18 keV was used with a high flux (10^{12} ph/s) and a 1 mm^2 beam size (1 × 1 mm^2 horizontal × vertical). The setup employed is a standard third-generation flat beam one, traditionally used on synchrotron imaging facilities associated to a 2D CCD detector. The CCD is the ESRF built Low noise/Fast Read-out FreLon Camera which employs a chip of 2000 × 2000 pixels 12 micrometers in size, coupled to a LAG (Lutetium Aluminium Garnet) scintillation screen by means of conventional Olympus optics (Koch et al. 1998, 1999). The transmission projections were recorded at 6 mm from the sample with an intrinsic resolution of 0.33 × 0.33 μm^2/pixel. Measurements of the camera point spread function (PSF) (Labiche et al. 1996; Koch et al. 1998, 1999), have yielded an overall resolution of about 0.8 μm or 2.5 pixels at maximum magnification. A 3D tomogram was obtained by reconstructing 2D slices, 0.33 μm apart, with the filtered backprojection algorithm (Kak and Slaney 2001). A set of 940 slices covers the entire sample. To reconstruct each slice, 625 projections were taken over an angle of 180° around the capillary axis, with an exposure time of 5 sec for each image. In order to extract quantitative information such as crack thicknesses or absorption coefficients, the reconstructed images were not corrected for ring artifacts. These corrections (Raven 1998) were applied only for the 3D rendering.

Fluorescence tomography. A monochromatic beam of 14 keV was used for this experiment, with a beam size of 2 × 10 micrometers (vert. × hor.). This was obtained using compound refractive lenses, together with a 10 μm diameter pinhole, for a flux of about 10^{10} ph/s on the sample. A PIN diode is placed in front of the sample to collect the incident flux for normalization purposes. Live time collected per point was about 1 second. The tomography was done in the vertical scanning geometry, recording 120 × 120 spectra (translations × rotations) with steps of 2.5 μm × 3°. The setup is a first-generation tomography one. Only a small fraction of the fluorescence emission can be detected because a pencil-beam and a single detector were used.

Fluorescence spectra were acquired on 2048 channels at each point of the scan using a Röntec Si-drift diode (SDD) detector placed in vertical geometry. This allows access to the highest spatial resolution available through the smaller vertical beam size (2 μm), with the relative penalty of increasing the scattering background compared to the standard setup (90° in the horizontal plane). The X-ray lines were fitted using an online version of the Axil program (Vekemans et al. 1994), which allows simultaneous analysis of characteristic elemental lines. For each detectable element in fluorescence, a 2D plot (sinogram) of its fluorescence intensity (background-free) as a function of the translation step and the rotation angle can be calculated.

The final images of the elemental maps were obtained from sinograms, using an iterative Algebraic Reconstruction Technique (ART) method (Simionovici et al. 2000), with a pixel size of 2.5 × 2.5 μm^2. In a general way, quantitative analyses of silicates are complicated by the attenuation length of the different fluorescence X-rays. Therefore, correction procedures, systematically applied in conventional 2D EPMA, have been developed for only a few particular sample geometries: either thin (Van Cappellen 1990) or infinite thickness layer (Chandler 1981), requiring a destructive sample preparation (polishing or slicing). The basis of the model used for the elemental reconstruction is the assumption that the matrix, composed of low-*Z* elements not recorded in fluorescence, can be neglected; that is, total attenuation is only caused by the elements measured in fluorescence. Thus, we can link measured total incident beam attenuation and fluorescent beam elemental attenuation, and solve the ART system of equations in an iterative manner. The mathematical formalism of the step-by-step absorption corrections applied, extrapolated from the one established for micrometer samples that do not require self-absorption corrections (Chukalina et al. 2002), is presented in Chukalina et al. (2003). Such an approach has the advantage of being independent of the a priori knowledge of the mineralogy of the studied assemblage. In addition, it could be implemented to take into account the fluorescence of "low *Z*" elements that could be detected with an instrumental setup adapted to this purpose.

RESULTS

Absorption tomography

The absorption X-ray tomography experiment shows that the grain is a heterogeneous assemblage. It is composed of two different phases having different X-ray absorption powers. On one reconstructed 2D tomographic section (Fig. 1a), the grain appears to have almost the same absorption power throughout the entire volume. Only a thin layer, having a slightly higher transmittance (Fig. 1a), was detected on a planar surface. The average thickness of the layer is about 5.6 ± 1.4 μm. Part of this layer appears detached from the grain (Fig. 1b). The 3D shape

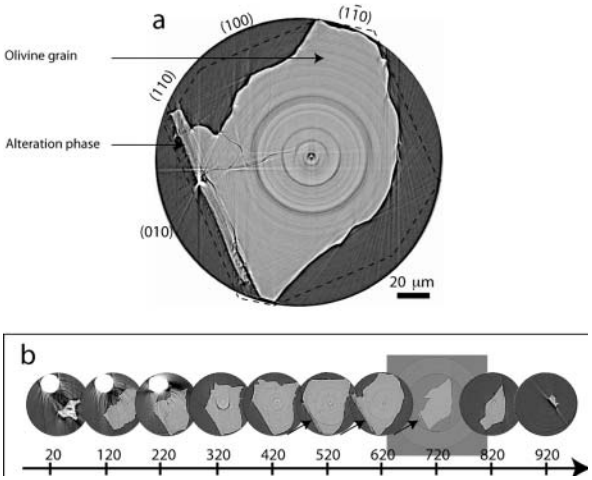

FIGURE 1. (**a**) A reconstructed absorption CT cross-section of a NWA817 grain viewed through a pure silica capillary. (**b**) Sequence of the Xth reconstructed cross sections sampled along the entire NWA817 grain every 33 µm perpendicularly to the capillary axis. To conserve maximum resolution, none of these images were filtered to remove the ring artifacts. With the exception of 720th section, only the images of the internal content of the capillary are reported in this Figure. The pure silica capillary has a 170 µm internal diameter, and 45 µm thick walls. The 650th section is the one reported in (**a**).

of the grain can be visualized using a stack of the reconstructed 2D tomographic sections (Figs. 1b and 2). The grain is elongated (315 µm against 170 µm) in the direction of the capillary. The 3D relative orientation of the planar surfaces observed in Figure 2 suggests that the grain is an olivine crystal, based on the law of constancy of interfacial angles proposed by Steno in 1669 and formulated by Romé de Lisle in 1772.

Proposed indexing of crystallographic faces is shown in Figure 1. The alteration layer is formed on a planar surface parallel to the axis of elongation. This surface is identified as the (010) face of the olivine crystal. The axis of elongation of the grain is the **c** axis. In olivine, the {010} plane has a good cleavage whereas {100} is an imperfect cleavage confirming the (010) indexation of this face (Fig. 1a). In a 3D visualization, the exact position of any detail of the grain in the silica container can be determined with respect to the goniometer head and also referenced relative to the strongly absorbing gold wire observed on the first sections in Figure 1b.

The absorption X-ray tomography experiment also reveals different kinds of internal surfaces. The intersections of the fracture surfaces with the studied section are visible as cracks on the reconstructed sections. No preferential "average" orientation of these cracks is seen in Figure 1, but many of the segments observed in the (001) plane are linear and oriented along the {010} and {100} cleavage lines. The segments look more like simple faults than veins because their thickness, if any, is less than 1 µm (<3 pixels). The internal network of fractures in the grain (dark contrast) and its topology can be examined throughout the entire sequence of slices (Fig. 1b) or in the tomogram (Fig. 2). Both the layer and the olivine are truncated by the same fractures, showing that the fracturing event post-dates the formation of the mineral assemblage.

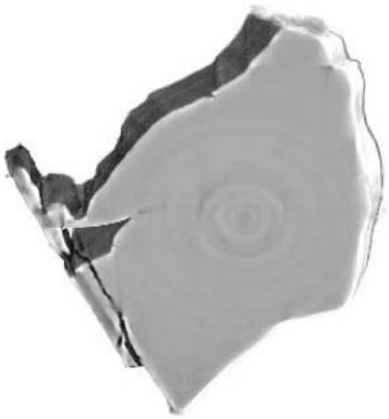

FIGURE 2. Three dimensional visualization of a 17 µm thick slice of the NWA817 grain, resulting from a stack of 51 reconstructed 2D tomographic sections. The 3D tomogram was reconstructed using the filtered backprojection algorithm (Kak and Slaney 2001) and the ring artifacts were filtered out on this representation. See text for description of the slice.

Fluorescence tomography

Fluorescence X-ray tomography analyses of the same section of the grain as the one presented in Figure 1 were recorded. The reconstructed sections were calculated using the Fe and Ca fluorescence signals. The Ca/Fe concentration ratio map calculated from these analyses is reported in Figure 3a. The variations of this ratio do not exceed 30% of the average value at the core of the section. The profiles of the Ca and Fe chemical composition measured along the green line marked in Figure 3a are reported in Figure 3b. The concentrations are normalized to the core composition.

A strong contrast of the Ca/Fe concentration ratios delineates a flat thin layer on the surface of the grain, corresponding to the thin "partly detached layer" observed by absorption tomography (Fig. 1). This layer is both enriched in Ca and Fe as shown in the chemical profiles reported in Figure 3b and has a Ca/Fe ratio 35% higher than the one of the contiguous olivine substrate. Its average apparent thickness is about 7.5 µm, but this value is certainly overestimated owing to the convolution with the 2 µm finite-sized beam spot. The thickness varies from 5 to 12.5 µm.

The entire bulk of the olivine grain, identified by absorption tomography, is affected by continuous variations in the Ca/Fe concentration ratios. The rims, having an average thickness of 20 µm, are relatively enriched in Fe. The chemical profiles show that this zoning can result either from a Ca depletion or from an Fe enrichment. The Ca and Fe chemical profiles are not symmetric and their variations are not readily connected. The variation of the Fe contents between the rims and the core can be as high as 20%, while the maximum variation of the Ca content is equal to 30%.

Electron images of transverse cuts

Backscattered electron images of the grain reveal that the sub-micrometer volume below the surface is heterogeneous. It is composed of two different phases characterized by slightly different average atomic numbers *Z* (Fig. 4). The one having the higher *Z* is the olivine,

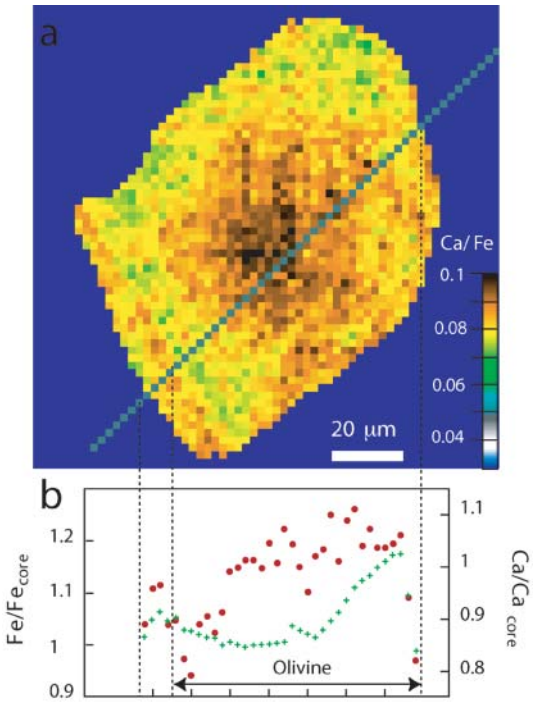

FIGURE 3. (**a**) The map of the Ca/Fe concentration ratio of a 10 µm thick section centered on the 650th section reported in Figure 1. It was calculated from the two tomographic cross-sections reconstructed from the fluorescence of Ca ($K\alpha$ = 3.7 keV) and Fe ($K\alpha$ = 6.4 keV). (**b**) Profiles of Fe (crosses) and Ca (solid circles) concentrations, detected along the grey line marked on (**a**) These concentrations are normalized versus an average concentration value measured in pixel no. 37 located in the core of the grain.

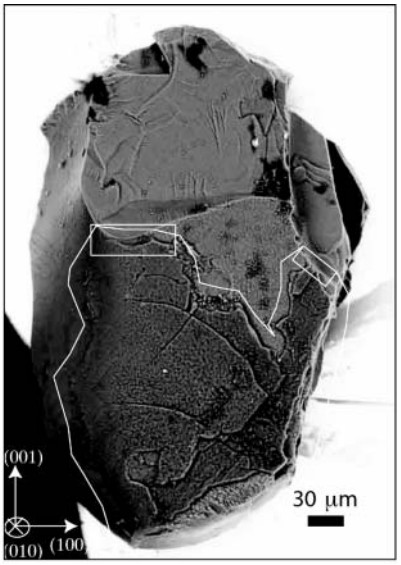

FIGURE 4. Back-Scattered Electron SEM image of the surface of a NWA817. The "reddish-phase" has a dark contrast; its contour is delineated by a white line. The two regions where FIB cuts were performed are indicated on the image with the presumed crystallographic axes of the olivine show at the left.

characterized by an orthorhombic symmetry, elongated along the **c** axis with conchoidal fractures. The other one with lower *Z* is layered and covers the (010) surface of the olivine grain.

The EDX analyses, carried out on the flattest surfaces of the sample not covered by the layered phase, indicate a chemical composition close to that of olivine ($Si/M^{2+} \sim 0.5$). This phase has a composition of $Fo_{40\pm0.5}$ ($Mg/Si \sim 0.75 \pm 0.5$) and contains less than 1 at% of Ca and Mn. In comparison, a stronger compositional variability was revealed by the analyses carried out on the layered phase, partly due to mixed contributions of different phases. This reddish layer is richer in silica ($0.8 \leq Si/M^{2+} \leq 1$) and contains a few at% of K and Al. It is also strongly depleted in Mg (< 7 at%) and Mn, whereas it is enriched in Ca. These results are consistent with the quantitative chemical analyses done on thin and planar sections reported in Sautter et al. (2002).

The SEM image reveals the 10 nm sub-surface of the grain. Observations of the olivine surface show, as expected, conchoidal fractures and a subhedral shape. The crystallographic orientation of the olivine grain is indicated in Figure 4. Observations of the "reddish" layer show it is thicker on the (010) surface of the olivine than on the other surfaces. It is composed of different superimposed strata and disrupted discontinuously (Fig. 5a). The external stratum contains numerous 500 nm pseudo-hexagonal crystals that are apparently embedded randomly (Fig. 5b) in a matrix. Below (or to the side of) this stratum, another stratum is present with microstructures oriented along a single direction (Fig. 5a). On fractures across the reddish layer, spontaneously formed during the extraction of the grain, the internal stratum always appears eroded, suggesting it has a lower hardness.

Two FIB cross cuts were prepared through an edge of the reddish layer formed on the (010) olivine surface, and their locations are indicated in Figure 4. The cuts were studied by SEM in SE and BSE modes (Fig. 5). In both cases, the differences in contrast enable one to distinguish a stratified layer formed on the olivine grain (Fig. 6). The average thickness of this layer is about 1 µm and it varies from 0 to 3.5 µm on the sample studied. The outer surface of the external stratum is decorated with nanometer-scale, pseudo-hexagonal crystallites. These crystallites cannot be seen beneath the outer surface, however, and may be present only on its exterior. At this scale, the contact between the external and the internal strata is diffuse but planar and continuous. A nanometer-sized porosity and a main fracture sub-parallel to the surface of the "reddish layer" are developed in the internal stratum. The thickness of this internal stratum is constant and equal to 1.5 µm. Its contact with the olivine grain appears irregular and occurs in a 300 nm thick layer.

DISCUSSION

3D nanopetrography of the alteration phase of the NWA817 meteorite

On the grain studied, the following sequence was observed: Fo_{40} olivine, Fa-rich olivine rim, a porous and fractured internal layer having a low average *Z* and a constant thickness, and a homogeneous external layer decorated by pseudo-hexagonal crystals. The boundary between the olivine and the porous layer is undulatory in a 300 nm layer (Fig. 6) and sub-parallel to the (010) olivine surface. This sequence and particularly the

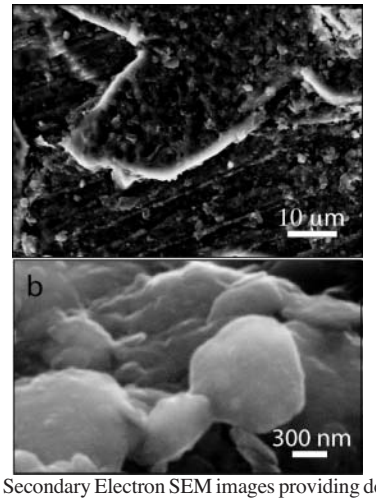

FIGURE 5. Secondary Electron SEM images providing detailed views of the "reddish-layer" observed on Figure 4. The stratification of the layer and the specific characteristics of the two strata can be observed in (**a**). A detailed view of nanometer crystals of the external stratum is shown in (**b**).

distribution of voids, first shown in this study, were obtained thanks to the specific FIB cut preparation. The SEM contrasts and the average chemical composition of the reddish phase ($0.8 \leq Si/M^{2+} \leq 1$) imply a high Si content of the internal layer and a high Fe content of the external layer. Neither the distribution of Ca on the nanometer scale nor the crystallinity of the two layers was resolved in this study. Finally, fractures intersect the entire sequence. For the sake of simplicity and in agreement with the observed distribution of the elements in the sequence, the following speculative mechanism of the formation of the secondary mineralization can be proposed:

$$(Mg_{0.4}Fe_{0.6})_2SiO_4 \rightarrow 0.8\ (MgSiO_3)_{\text{internal layer}} + 1.2\ (FeO)_{\text{external layer}} + 0.2\ (SiO_2)_{\text{fluid}} \quad (1)$$

Indeed, a preferential removal of fayalite from the olivine could lead to the formation of a residual Fe-poor and Si-rich internal layer (labeled "$MgSiO_3$" in Eq. 1) having abundant voids in its destabilized structure. Above this internal layer, fluids enriched by the fayalite components could partly precipitate an FeO-rich external layer (labeled "FeO" in Eq. 1). Note that Equation 1 does not presuppose any information about the crystallinity of the products.

These data reported on the nanometer scale can be compared to some extent with data on the alteration phase formed in a vein found in olivine from the meteorite Lafayette (Harvey and McSween 1992; Treiman 1993; Vicenzi et al. 1997; Vicenzi and Heaney 1999). The following assemblage was observed (Vicenzi et al. 1997): a porous-amorphous Fe-Ca-rich phase having a low electron transmittance (corresponding to a high average *Z*); an amorphous Si-rich phase having a high electron transmittance; and an assemblage of Fe-oxide/Fe-oxyhydroxide with phyllosilicates. The contact between the two amorphous phases is undulatory and occurs on a 300 nm layer. It can thus be concluded that the alteration phase of the NWA817 is neither anomalous nor original in comparison to other aqueous phases formed on Fe-rich olivines.

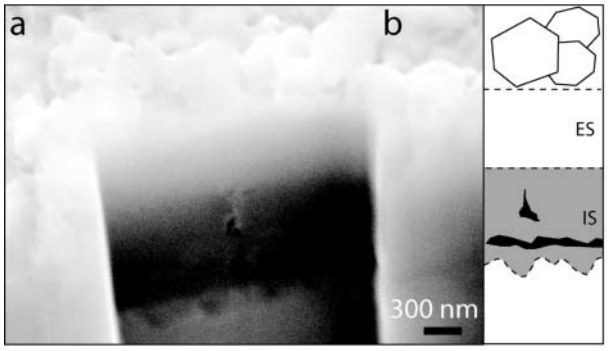

FIGURE 6. Secondary Electron SEM image of a FIB cut across the stratified "reddish layer" (tilt ~ 60°) (**a**) and a schematic view (**b**). Within the internal stratum (IS) both the porosity and the fracture are shown in black, the external stratum is marked as ES. See text for discussion of structures.

Potential of X-ray absorption and fluorescence CT combination for determining 3D mineralogy

The comparison between the X-ray and electron analyses on the NWA817 olivine grains is presented above to discuss the information that can be obtained from the computed images by the X-ray tomographies applied to the sub-millimeter grains stored in a silica capillary.

Mineralogy and X-ray absorption CT. The 3D absorption reconstruction of the assemblage allows the identification, by means of the law of the constancy of interfacial angles, of the main grain of the assemblage as an olivine crystal. The absorption reconstructions obtained with the current setup discriminate between the olivine phase and the thin alteration layer because of the difference in their linear attenuation coefficients μ (cm^{-1}) defined as follows:

$$\mu = \rho \sum_i \chi_i \cdot \sigma_i \quad (2)$$

where ρ is the density, χ_i is the weight concentration, and σ_i is the absorption coefficient of the i^{th} element of the probed phase. No contrast is observed in zones corresponding to the thin alteration layer and olivine, contrary to electron analyses (Fig. 6 and Sautter et al. 2002). Considering that a relative difference of μ can be observed if it is higher than the statistical uncertainty estimated from Figure 1 (about 6%), we can establish a 3 cm^{-1} sensitivity. The values of the linear attenuation coefficient of the olivine ($\mu = 52 \pm 6$ cm^{-1}) and of the alteration layer ($\mu = 40 \pm 5$ cm^{-1}) are estimated from the measured grey level contrasts on zones free of ring artifacts, and the known relative difference of μ between the air and the silica capillary ($\Delta\mu = 6.9$ cm^{-1}).

The linear attenuation coefficient of the Fo_{44} olivine core composition ($\mu = 53.7$ cm^{-1}) and of an Fo_{38} olivine, which is the average chemical composition of the olivine having the chemical profiles reported in Figure 3b ($\mu = 56.5$ cm^{-1}), can be calculated using the EPMA compositions (Sautter et al. 2002) and the photon scattering cross-sections of Hubbell et al. (1974). We verify that all of the values of the linear attenuation coefficients of the olivine, calculated and measured, are undistinguishable using the stated sensitivity. Conversely, an $Fo_{45\pm9}$ olivine chemical composition can be estimated from the measured attenuation coefficient

by means of the following numerical formula:

$$\mu(x) = \frac{(17486.87 - 20187.5x + 3868.7x^2 + 0.04x^3)}{(204 - 64x)} \quad (3)$$

where x is the forsterite content of the olivine. This formula is calculated assuming the olivine belongs to the forsterite-fayalite series, using Equation 2 and the Fisher-Medaris equation relating the density to the forsterite content (Brown 1982) and the photon scattering cross-sections of Hubbell et al. (1974). Furthermore, using the EPMA composition and the measured attenuation coefficient of the alteration phase, an average density of 3.5 ± 0.4 g/cm^3 can be predicted for the alteration phase. For any mineral of the silicate family, the linear attenuation coefficient is in the range of 85 to 6.9 cm^{-1} for fayalite and quartz, respectively. Given the achieved sensitivity, a set of mineralogical predictions can be formulated for any silicate phase stored in a silica capillary.

Mineralogy and X-ray fluorescence CT. Chemical compositions determined using the current setup cannot be fully quantitative for several reasons. First, elements having $Z < 14$, such as C, O, Mg, and Al, are not detectable with the Röntec Si-drift diode (SDD) detector used in the setup dedicated to fluorescence tomography. This limitation could be partially circumvented by adapting the instrumental setup to "low Z" quantitative analysis purposes by encasing the sample stage and detector in a vacuum or He-filled chamber. Second, the effect of imprecision of the voxel size of the reconstructed images renders the estimate of the absolute number of fluorescent atoms per unit volume difficult. However, semi-quantitative analyses based on the elemental composition ratio determination can be performed, since they are independent of the voxel size. Intensity ratios measured in the same detection geometry also allow minimizing the effects of the setup.

The applied reconstruction procedure (Chukalina et al. 2003) is a complex mathematical problem related to the general class of inverse problems, for which a full treatment of the uncertainties of the reconstructed parameters has not yet been proposed. In the following, the reconstructed concentration ratios will be compared to the EPMA results in order to validate them. It is verified that the low-Z elements, neglected in the applied reconstruction calculation, produce less than 15% of the attenuation of the incident beam in a 100 micrometer sized Fo_{44} olivine. The reconstructed Ca and Fe concentrations are not linearly related and their profiles are not radially symmetric, indicating that they do not result from geometrical artifacts. Furthermore, the X-ray attenuation lengths of the Ca and Fe fluorescence in the Fo_{44} are 9 ± 0.2 and 42 ± 1 µm, respectively, and different from the 20 µm thickness of the rims estimated from figure 3b. This data supports the fact that the observed profiles do not result from self-absorption. The Fe content of one of the studied rims is 20% higher than in the core, whereas the maximum variation of the Ca content is 30%. All these characteristics are in agreement with the data previously established by EPMA analyses. Indeed, the reported rim to core maximum chemical variation is 33% for Fe and 75% for Ca content. However, the reconstructed absolute value of the Ca/Fe ratio of the bulk olivine (Ca/Fe ~ 0.1) appears 10 times larger than the value averaged over 20 EPMA analyses (see $Ca/Fe_{core} = 0.015$, Sautter et al. 2002). For the reconstruction procedure, the measured transmission of the beam is used for normalizing the iteratively calculated concentrations of the Ca and Fe elements. If the low Z elements are neglected, the variation of the Fe content required to obtain the same transmission as for a 100 micrometer-sized Fo_{44} olivine grain is less than 15%. This variation can be considered the maximum absolute uncertainty on the Fe concentration and it is certainly minimized in the iterative process. In this case, the Ca/Fe ratio is about 0.008. If the transmission is compensated by the addition of Ca in an olivine-like lattice containing only the Fe content of an Fo_{44}, then Ca/Fe is equal to about 0.3. Although the reconstructed value of the Ca/Fe ratio appears 10 times too high, it is within the range of variation of the Ca/Fe ratio.

To conclude, the combination of the interpretations of the absorption and fluorescence X-ray tomographic results leads to the same petrographic and mineralogic understanding of the assemblage of one grain as the one established by the electron techniques. The precision achieved, although moderate, is sufficient to obtain a semi-quantitative 3D view of the mineralogy. Indeed, the assemblage is mainly composed of a few hundreds of micrometer thick, subhedral olivine grains and of a few micrometers-thick surface layer. The olivine grain has irregular chemical profiles, with rims enriched in Fe and or depleted in Ca. The thin layer has numerous common properties with leached layers. Indeed, it is observed on one specific face of the olivine crystal. The elements detected in this layer are also in the olivine. Finally, the layer must have a lower density than the olivine in order to explain its relative elemental enrichment in Fe (observed by fluorescence CT) and its attenuation coefficient significantly lower than the olivine one (observed by absorption CT). Alteration of the olivine grain is thus a mechanism that could be proposed to explain the formation of the studied layer. A network of fractures is distributed over the entire assemblage.

Furthermore, this combination of tomographies with a beam of a few tens of keV emitted by a third-generation synchrotron source gives rise to a nondestructive and noninvasive 3D semi-quantitative microprobe assay adapted to study the mineralogy of sub-millimeter silicate grains in a container. The sequential application of the X-ray micro-fluorescence probe, possibly coupled to other X-ray microprobes (i.e., X-ray diffraction), followed by scanning and transmission electron microscopies coupled with the FIB technique under partial vacuum, is a possible methodology to deliver an unequivocal and more quantitative 3D petrographic and mineralogic description.

ACKNOWLEDGMENTS

We thank S. Borensztajn and L. Beaunier (Laboratoire de Physique des Liquides et Electrochimie de Paris, UPR15 du CNRS) for SEM images. The manuscript benefited from the careful reading and the constructive comments of S. Sheppard and F. Robert; we warmly thank them. This work was supported by the CNES through the DAR no. 793/2001/CNES/8995 and was also performed partly under the auspices of the NATO Scientific Affairs Division, through grant no. EST-CLG-979530.

REFERENCES CITED

Boisseau, P. and Grodzins, L. (1987) Fluorescence tomography using synchrotron radiation. Hyperfine Interactions, 33, 283–292.

Brown, G.E. Jr. (1982) Olivines and silicate spinels. In P.H. Ribbe, Ed., Orthosilicates (2nd ed.) 5, 275–381. Reviews in Mineralogy, Mineralogical Society of America, Washington, D.C.

Chandler, J.A (1981) Quantitative X-ray microanalysis. In A.M. Glauert, Ed., X-ray microanalysis in the electron microscope, p. 471–494. Amsterdam,

New-York, Oxford.
Chukalina, M., Simionovici, A., Snigirev, A., and Jeffries, T. (2002) Quantitative characterization of microsamples by X-ray fluorescence tomography. X-Ray Spectrometry, 31, 448–450.
Chukalina, M., Simionovici, A., Lemelle, L., Rau, Ch., Vincze, L., and Gillet, P. (2003) X-ray fluorescence tomography for nondestructive semi-quantitative study of microobjects. Journal de Physique IV France, 104, 627–630.
Flynn, G.J., Rivers, M., and Sutton, S.R. (2000). X-ray computed microtomography (CMT): a non-invasive screening tool for characterization of returned rock cores from Mars and other solar system bodies. 31th Annual Lunar and Planetary Science Conference, Abstract No. 1893, Houston, Texas.
Gillet, Ph., Barrat, J.A., Deloule, E., Wadhwa, M., Jambon, A., Sautter, V., Devouard, B., Neuville, D., Benzerara, K., and Lesourd, M. (2002) Aqueous alteration in the Northwest Africa 817 (NWA817) Martian meteorite. Earth and Planetary Science Letters, 203, 431–444.
Harvey, R.P. and McSween, H.Y. Jr. (1992) The parent magma of the nakhlite meteorites: clues from melt inclusions. Earth and Planetary Science Letters, 111, 467–482.
Heaney, P.J., Vicenzi, E.P., Gianuzzi, L.A., and Livi, K.J.T. (2001) Focused ion beam milling: a method of site-specific sample extraction for microanalysis of Earth and planetary materials. American Mineralogist, 86, 1094–1099.
Hubbell, J.H, McMaster, W.H., Del Grande, N.K., and Mallett, J.H. (1974) X-Ray Cross Sections and Attenuation Coefficients. In J.A. Ibers and W.C. Hamiliton, Eds., IUCr International Tables for X-Ray Crystallography, p. 47–70. Kynoch Press, Birmingham. Based on McMaster, W.H., Del Grande, N.K., Mallett, J.H., and Hubbell, J.H. (1969) Compilation of X-Ray Cross Sections. Lawrence Livermore National Laboratory Report UCRL-50174, Sec II, Rev.1.
Kak, A.C. and Slaney, M. (2001) Principles of Computerized Tomography Imaging, 322p. In Classics in Applied Mathematics, 33, SIAM, Philadelphia, US.
Ketcham, R.A. and Carlson, W.D. (2001) Acquisition, optimization and interpretation of X-ray computed tomographic imagery: Applications to the geosciences. Computers and Geosciences, 27, 381–400.
Koch, A., Raven, C., Spanne, P., and Snigirev, A. (1998) X-ray imaging with submicrometer resolution employing transparent luminiscent screens. Journal of the Optical Society of America, 15, 1940–1951.
Koch, A., Peyrin, F., Heurtier, P., Ferrand, B., Chambaz, B., Ludwig, W., and Couchaud, M. (1999) X-ray camera for computed microtomography of biological samples with micrometer resolution using $Lu_3Al_5O_{12}$ and $Y_3Al_5O_{12}$ scintillators. In J.H. Beene and J.T. Dobbins, Eds., Physics of Medical Imaging. SPIE Proceedings, 3659, 170–178.
Labiche, J.C., Segura Puchades, J., Brussel, D.V., and Moy, J. (1996) FRELON Camera: fast readout low noise. ESRF Newsletter, 25, 41–43.
Lemelle, L., Abel, F., Cohen, C., and Guyot, F. (2002) Study of the (010) olivine surface by Rutherford backscattering spectrometry in channeling geometry. American Mineralogist, 87, 327–332.
McSween, H.Y. (1994) What we have learned about Mars from SNC meteorites. Meteoritics, 29, 757–779.
Rau, Ch., Weitkamp, T., Snigirev, A., Schroer, C.G., Tümmler, J., and Lengeler, B. (2001) Recent developments in hard X-ray tomography. Nuclear Instruments and Methods in Physics Research, Section A-Accelerators Spectrometers Detectors and Associated Equipment, A467-468, 929–931.
Raven, C. (1998) Numerical removal of ring artifacts in microtomography. Review of Scientific Instruments, 69, 2978–2980.
Raven, C., Snigirev, A., Koch, A., Snigireva, I., and Kohn, V. (1997) X-ray tomography with micrometer spatial resolution. In U. Bonse, Ed., Developments in X-ray Tomography. SPIE Proceedings, 3149, 140–148.
Sautter, V., Barrat, J-A., Jambon, A., Javoy, M., Lorand, J.P., Gillet, P., Joron, J.L., and Lesourd, M. (2002) A new Martian meteorite from Morocco: the nakhlite North West Africa 817. Earth and Planetary Science Letters, 6087, 1–16.
Schroer, Ch., Benner, B., Günzler, Tf., Kuhlmann, M., Lengeler, B., Schröder, W.H., Kuhn, A.J., Simionovici, A., Snigireva, A., and Snigireva, I. (2001) High resolution element mapping inside biological samples using fluorescence microtomography. In U. Bonse, Ed., Developments in X-ray tomography III. SPIE Proceedings, 4503, 230–239.
Simionovici, A., Chukalina, M., Schroer, C., Drakopoulos, M., Snigirev, A., Lengeler, B., Janssens, K., and Adams, F. (2000) High-resolution X-ray fluorescence microtomography of homogeneous samples. IEEE Transactions on Nuclear Science, 47, 2736–2740.
Simionovici, A., Chukalina, M., Vekemans, B., Lemelle, L., Gillet, P., Schroer, C., Lengeler, B., Schröder, W., and Jeffries, T. (2001) New results in X-ray computed fluorescence tomography. In U. Bonse, Ed., Developments in X-ray tomography III. SPIE Proceedings, 4503, 222–229.
Sutton, S.R., Flynn, G.J., Rivers, M., Newville, M., and Eng, P. (2000) X-ray fluorescence microtomography of individual interplanetary dust particles. 31st Annual Lunar and Planetary Science Conference, Abstract No. 1189, Houston, Texas.
Treiman, A.H., Barrett, R.A., and Gooding, J.L. (1993) Preterrestrial aqueous alteration of the Lafayette (SNC) meteorite. Meteoritics, 28, 86–97.
Van Cappellen, E. (1990) The parameterless correction method in X-ray microanalysis. Microscopy Microanalysis Microstructures, 1, 1–22.
Vekemans, B., Janssens, K., Vincze, L., Adams, F., and Van Espen, P. (1994) Analysis of X-ray spectra by iterative least squares (AXIL): new developments. X-ray Spectrometry, 23, 278–285.
Vicenzi, E.P. and Heaney P.J. (1999) Examining Martian alteration products using in situ TEM Sectioning: A Novel application of the focused ion beam (FIB) for the study of extraterrestrial materials. 30th Annual Lunar and Planetary Science Conference, Abstract No. 2005, Houston, Texas.
Vicenzi, E.P., Tobin, K., Heaney, P.J., Onstott, T.C., and Chun, J. (1997) Carbonate in Lafayette Meteorite: A Detailed Microanalytical Study. Meteoritics and Planetary Science, 32, A132.

MANUSCRIPT RECEIVED JUNE 12, 2003
MANUSCRIPT ACCEPTED NOVEMBER 24, 2003
MANUSCRIPT HANDLED BY ROBERT DYMEK